

Constraints on Neutrino Mass with Void Weak Lensing Effect

Wenshuo Xu,^{1,*} Cheng Zhao,^{1,†} Chen Su,^{2,3} Huanyuan Shan,^{2,3} and Yu Liu^{1,4}

¹*Department of Astronomy, Tsinghua University, Beijing 100084, China*

²*Shanghai Astronomical Observatory (SHAO), Nandan Road 80, Shanghai 200030, China*

³*University of Chinese Academy of Sciences, Beijing 100049, China*

⁴*Institute of Physics, Laboratory of Astrophysics,
École Polytechnique Fédérale de Lausanne (EPFL),
Observatoire de Sauverny, CH-1290 Versoix, Switzerland*

(Dated: March 11, 2026)

Cosmic voids, the underdense regions of the Large Scale Structure (LSS), provide cosmological information highly complementary to that obtained from overdense regions. In this work, we investigate the constraining power of the void–shear cross-correlation (void lensing effect) on the total neutrino mass. Based on cosmological simulations with varying neutrino masses, we identify voids with the DIVE void finder and obtain their density profiles from the underlying dark matter and neutrino distributions. We then generate mock shear catalogues through ray-tracing and measure the corresponding void lensing signals. Our results show that void lensing yields an independent constraint on total neutrino mass as $\sigma(M_\nu) = 0.096 \text{ eV}$ in the absence of shape noise, and $\sigma(M_\nu) = 0.340 \text{ eV}$ when adopting a Stage-III-like shape noise ($\sigma_e \simeq 0.3$). Moreover, we find a clear linear relationship between the void lensing signal and neutrino mass. We further validate the forward modelling of the void lensing signal from the void density profiles across different cosmologies, demonstrating its accuracy and potential for future applications. These findings highlight void lensing as a promising probe of massive neutrinos and motivate its applications to galaxy survey data as well as the combination with other cosmological observables.

I. INTRODUCTION

As a standard cosmological paradigm, the Λ CDM model succeeds in fitting a number of independent observations. Experiments on the Cosmic Microwave Background (CMB) anisotropies provide tight constraints on the six Λ CDM parameters [1–3], while other low-redshift probes make further improvements by breaking parameter degeneracies. However, there are still remaining open questions for the Λ CDM model (e.g. Ref. [4]). Meanwhile, with the increasing volume and tracer density of cosmological surveys, more attention has been devoted to extensions of the vanilla Λ CDM model, including dynamical dark energy (e.g. Ref. [5]), modified gravity (e.g. Ref. [6]), primordial non-Gaussianity (e.g. Ref. [7]) and massive neutrinos (e.g. Ref. [8]).

The state-of-the-art constraints on total neutrino mass ($M_\nu = \Sigma m_\nu$) arise from the combination of particle physics experiments and cosmological observations. The recent KATRIN experiment places an upper limit of $M_\nu < 1.35 \text{ eV}$ (90% C.L.) when combined with neutrino oscillations [9], while oscillation experiments further set lower limits for the two possible mass orderings [10]. In parallel, cosmological constraints on neutrino mass have also steadily tightened (e.g. Refs. [8, 11–13]). As massive neutrinos remain relativistic until relatively late time and further suppress the growth of small-scale density perturbations through free streaming, they leave imprints on both the cosmic expansion history and large-scale

matter distribution. Using Baryon Acoustic Oscillations (BAO) measurements to constrain the expansion history, the Dark Energy Spectroscopic Instrument (DESI) Collaboration has reported the tightest constraint to date as $M_\nu < 0.0642 \text{ eV}$ (95% C.L.) when combined with CMB data [8, 14]. However, this result is known to be affected by prior weight effects, with the data favoring negative mass values when incorporating the effective cosmological neutrino mass parameter [15]. Such tension implies potential unknown systematics or new physics, such as dynamical dark energy [8]. While these constraints all rely on the cosmic expansion history, neutrino free-streaming effect can provide complementary information, which is manifested as a scale-dependent suppression of the power spectrum [16–18]. Beyond the 2-point clustering of galaxies, several higher-order probes sensitive to neutrino free-streaming have also been proposed to constrain massive neutrinos, such as the bispectrum [19, 20], Minkowski functional [21, 22], persistent homology [23–25] and cosmic voids [26–28].

Cosmic voids, which trace underdense regions of the LSS and constitute most of the volume in the Universe, have been shown to provide complementary cosmological information to that from overdense regions [29–34]. Unlike gravitationally collapsed structures, voids still mostly maintain linear evolution features and are marginally affected by baryonic effects [35, 36]. This suggests voids to be powerful probes of several cosmological effects, such as dark energy [37, 38], modified gravity [39, 40], primordial non-Gaussianity [41] and massive neutrinos [26].

Owing to their large thermal velocities, massive neutrinos are less clustered than cold dark matter, leading to a relatively higher neutrino fraction in under-

* xws21@mails.tsinghua.edu.cn

† czhao@tsinghua.edu.cn

dense regions. This makes voids a promising environment to constrain neutrino properties (e.g. Refs. [26–28, 42, 43]). Ref. [26] performed the first systematic study of cosmic voids in massive neutrino cosmologies and found that, with the presence of massive neutrinos, voids tend to present larger sizes, higher ellipticities, less empty inner densities and smaller radial velocity magnitudes. They also showed that these differences become less pronounced at higher redshifts, as neutrinos are more relativistic and less affect the structure formation. In particular, based on these results, the authors proposed the void density profile as a sensitive probe of neutrino mass and further discussed the challenges of theoretical modelling in Ref. [44].

From the observational perspective, an additional challenge in using void density profiles for cosmological constraints arises from that the distributions of dark matter and neutrinos inside voids cannot be directly observed. Several works (e.g. Refs. [45, 46]) have tried to use galaxies as biased tracers of underlying matter distribution but require careful modelling of galaxy bias. In contrast, gravitational lensing, as a purely gravitational effect, provides a direct probe of the total matter distribution [47]. In the weak lensing regime, lensing shear measurements enable to both constrain the matter distribution around specific foreground lens objects and probe the large-scale matter distribution in the Universe [48–50]. Following this idea, the weak lensing effect of cosmic voids facilitates the measurement of void density profile.

The weak lensing effect of cosmic voids has been extensively studied. Observationally, void lensing signals have been detected through the cross-correlation between lensing catalogues and voids identified in photometric or spectroscopic galaxy surveys (e.g. Refs. [51, 52]). Recently, Ref. [53] reported the highest-significance detection to date of a 6.2σ -measurement using spectroscopically identified voids in SDSS-III BOSS and UNIONS lensing shear catalogues. Theoretically, void lensing has also been widely shown to be sensitive to modifications of gravity, owing to the reduced screening effect in underdense environments [40, 54, 55]. Nevertheless, only a limited number of studies have investigated the response of void lensing to massive neutrinos (e.g. Refs. [27, 56]), and the constraining power of void lensing is still largely unexplored.

In practice, void studies are further complicated by the emergence of multiple void-finding algorithms, owing to the absence of an explicit definition for void spatial boundaries. Most algorithms rely on triangulation or tessellation (e.g. Refs. [57–59]), while some others adopt numerical estimation of the local density contrast [60]. Ref. [61] also proposed the direct construction of voids in lensing convergence maps. As voids defined in different ways can exhibit different properties [62, 63], it is important to choose the definition providing adequate information for specific studies.

In this work, we adopt the DIVE void finder developed in Ref. [64]. The resulting Delaunay Triangulation (DT)

voids have been shown to achieve a high statistical S/N ratio [38, 65], which benefits our void lensing analysis. Using N -body simulations with varying total neutrino masses, we investigate the constraining power of DT-void lensing effect on neutrino mass and provides a quantitative forecast based on posterior sampling. In addition, we develop the forward theoretical modelling of lensing signal from the void density profile.

This paper is structured as follows: We present the basic formalism of weak lensing in Section II, and introduce the simulation data and methods used to generate mocks in Section III. Then Section IV shows the measurements of void density profiles and weak lensing signals from our simulation and mock data. Finally, we provide the inference on neutrino mass in Section V, and discuss our results and conclude in Section VI.

II. WEAK LENSING FORMALISM

In this section, we briefly review the formalism of weak gravitational lensing and the derived equations related to this work. More comprehensive reviews can be found in Refs. [47] and [66].

When light from distant galaxies propagates through the foreground large-scale structures, its path is perturbed by the gravitational field. In the weak lensing regime, this deflection effect induces distortions in the observed shape of distant galaxies, which can be described by the Jacobian matrix:

$$A = \begin{pmatrix} 1 - \kappa - \gamma_1 & -\gamma_2 \\ -\gamma_2 & 1 - \kappa + \gamma_1 \end{pmatrix} \quad (1)$$

, where the *convergence* κ indicates the overall size magnification, while the *shear* γ_1 and γ_2 describe the change in ellipticity.

When isolating the weak lensing effect of an axially symmetric foreground lens (such as DT voids in this work; see Section III B 2), its convergence profile can be expressed in thin-lens approximation as

$$\kappa(R) = \frac{\bar{\rho}_{m,0}}{\Sigma_{c,\text{comov}}} \int \delta(r = \sqrt{R^2 + z^2}) dz, \quad (2)$$

where R is the 2D projected radius, δ is the overdensity and $\Sigma_{c,\text{comov}} = \frac{c^2}{4\pi G} \left[\frac{\chi_s a_l}{(\chi_s - \chi_l)\chi_l} \right]$ is the *comoving* critical surface mass density. Here the subscripts s and l stand for the source and lens, respectively, and χ is the comoving distance. The shear effect around the foreground lens can be further transferred to the tangential (γ_t , E-mode) and cross (γ_\times , B-mode) terms, and the tangential component is approximated by the convergence as

$$\gamma_t(R) = \bar{\kappa}(< R) - \kappa(R), \quad (3)$$

where $\bar{\kappa}$ is the convergence averaged within a given radius, $\bar{\kappa}(< R) = 2/R^2 \int_0^R r \kappa(r) dr$. A generally chosen

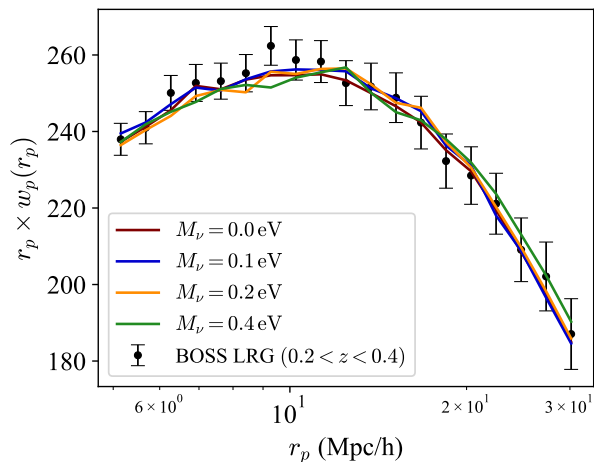


FIG. 1. The results of HOD fitting. Lines in different colors indicate the best-fit projected 2-point correlation function in simulations with different neutrino masses. The black data points show the projected clustering of BOSS LRGs in $0.2 < z < 0.4$ and the errorbars are estimated with 1000 PATCHY mocks.

measurement in observations is the excess surface mass density (ESD) $\Delta\Sigma$, which is defined as

$$\Delta\Sigma(R) = \Sigma_{c,\text{phys}}\gamma_t = \Sigma_{c,\text{phys}}(\bar{\kappa} - \kappa), \quad (4)$$

where the *physical* critical surface mass density $\Sigma_{c,\text{phys}} = \frac{c^2}{4\pi G} \frac{D_s}{D_l^2 D_t} = \Sigma_{c,\text{comov}}/a_l^2$, D represents angular diameter distance and a_l is the scale factor at the redshift of foreground lens. $\Delta\Sigma$ reflects the projected mass distribution around the lens objects and maximizes the S/N ratio of measurement by weighting sources at different redshifts with critical surface density [67].

Eqs. (2)-(4) clarify the relations between lens density profile and weak lensing signal, which indicates we can constrain the density profile through weak lensing measurements, as well as theoretically forward model the lensing signal from density profile. When processing simulation and mock data, density profile can be measured through the cross-correlation between voids and dark matter and we adopt the estimator of $\Delta\Sigma$

$$\widehat{\Delta\Sigma} = \frac{\Sigma_{i,j} w_{ij} e_{t,ij} \Sigma_{c,ij}}{\Sigma_{ij} w_{ij}}, \quad (5)$$

where the tangential ellipticity of source galaxies e_t works as an unbiased estimator of the lensing tangential shear γ_t in Eq. (4). The weight function w_{ij} is assigned to each lens-source pair to improve the statistical S/N in observational studies [68, 69]. In this simulation-based work, we set $w_{i,j} = 1.0$ for simplicity.

III. SIMULATIONS AND MOCKS

In this section, we present the data and methods used to generate mocks. We first introduce the setup of our N -

body simulations with different neutrino masses in Section III A, then discuss the mock DT void catalogues in Section III B. Finally, Section III C presents our raytracing pipeline and the incorporation of observational effects.

A. N -body Simulations with Massive Neutrinos

To investigate the impact of massive neutrinos on the void lensing signal, we employ four N -body simulations with different total neutrino masses. We use the $M_\nu = 0.0$ and 0.1 eV realizations from *Jiutian* extension runs [70], and generate two additional realizations with $M_\nu = 0.2$ and 0.4 eV in the same manner using the publicly available information-optimized code CUBE [71, 72].

These simulations co-evolve cold dark matter and neutrinos in a cubic box of side length 1500 Mpc/h with periodic boundary conditions, using $N_{\text{part}} = 2048^3$ dark matter particles. To avoid the shot noise problem of neutrinos, we adopt the grid-based method and evolve massive neutrinos on a mesh with $N_{\text{pix}} = 2048^3$.

For the two additional runs, we use the same initial Gaussian random field as the two from *Jiutian* to cancel the impact of cosmic variance on our analyses, and adopt *Planck2018* cosmology [1]: $\Omega_m = 0.3111$, $h = 0.6766$, $n_s = 0.9665$ and $A_s = 2.100549 \times 10^{-9}$. For simulations with massive neutrinos, we include a non-zero Ω_ν and reduce Ω_{cdm} to make the total matter density invariant. Then the initial power spectrum and transfer functions are recalculated with CAMB [73].

B. Void Catalogue

In this work, we simulate voids identified from galaxy 3D positions, which can be measured in spectroscopic surveys. For simplicity, we only study voids around $z_l = 0.3$.

From N -body simulations, we adopt the ROCKSTAR halo finder [74] to generate catalogues of halos with more than 20 dark matter particles, corresponding to a lower limit of halo mass around $6.8 \times 10^{11} M_\odot/h$. Then we populate galaxies according to the clustering of BOSS LRG galaxies in $0.2 < z < 0.4$ through the vanilla HOD model (Section III B 1). Finally, we identify void catalogues from galaxies with the DIVE void finder (Ref. [64], and briefly reviewed in Section III B 2).

1. Halo Occupation Distribution (HOD)

In this work, we generate galaxy catalogues from dark matter halos with the vanilla five-parameter HOD model introduced in Ref. [75]. In HOD models, galaxies are separated into central and satellite galaxies. The occupation of central galaxies is assumed to follow a Bernoulli

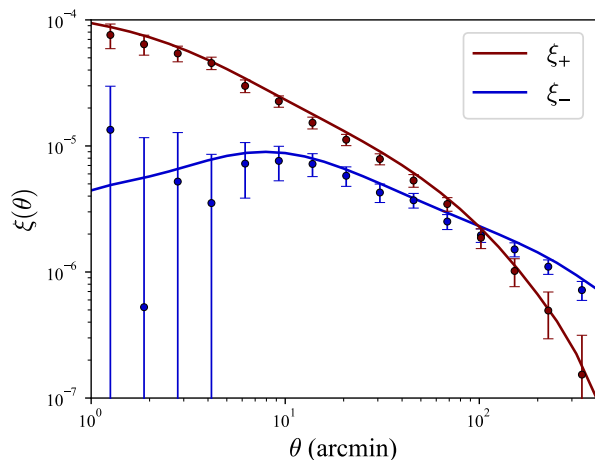


FIG. 2. Shear auto-correlation functions ξ_+ (red) and ξ_- (blue). The data points are the measurements in our mock source catalogues using TRECCORR [80] and the errorbars are estimated in 15 realizations (see Section V B). Here we incorporate a shape noise $\sigma_e = 0.3$ in the catalogues. The solid lines are the prediction of 3D matter power spectrum calculated with PYCCL [81].

distribution described by M_{\min} and $\sigma_{\log M}$, while satellites follow a Poisson distribution with M_0 , M_1 and α . We refer interested readers to the original paper for the specific formulae.

As we only focus on voids around $z = 0.3$ in this work, we measure the projected 2-point correlation function $w_p(r_p)$ of SDSS-III BOSS LRG galaxies at $0.2 < z < 0.4$ (LOWZ samples in Ref. [76]) and use it as the data vector in HOD fitting. The projected correlation function, which is the compressed redshift-space 2-point correlation function $\xi(r_p, r_\pi)$, can be expressed as

$$w_p(r_p) = 2 \int_0^{r_{\pi, \max}} \xi(r_p, r_\pi) dr_\pi, \quad (6)$$

where r_p and r_π are the transverse and light-of-sight separations, respectively. In this work, we use the Landy & Szalay estimator [77]:

$$\xi(r_p, r_\pi) = \frac{DD - 2DR + RR}{2}, \quad (7)$$

where R is the random catalogue, and we calculate the integration in Eq. 6 with $r_{\pi, \max} = 35 \text{ Mpc/h}$. The covariances used for HOD fitting are estimated with 1000 PATCHY mocks [78]. We present the HOD fitting results in Fig. 1, which indicates a great fit in all four simulations. Then with the best-fit HOD parameters, we populate mock galaxies with HALOTOOLS [79], and randomly downsample the four galaxy catalogues to the same number density $3 \times 10^{-4} \text{ Mpc}^{-3} h^3$ to keep aligned with BOSS galaxies. In addition, as the DT voids are defined in a geometric way, a higher tracer number density will systematically suppress the abundance of large voids, which can be avoided with the downsampling.

2. Void Finder

In this work, we employ the Delaunay trIangulation Void findER (DIVE) developed in Ref. [64], which samples underdense regions using the circumferences of the Delaunay Triangulation of tracers. The *DT voids* identified with DIVE show a large overlapping fraction, leading to a high number density. The clustering measurement of DT voids shows this high density results in an improved S/N ratio for statistical studies [38, 65]. We identify voids from the galaxy catalogues described in Section III B 1 with DIVE and use the original overlapping void catalogues in the analysis. Moreover, the spherical shape and naturally defined void radius of DT voids further facilitate the theoretical modelling of lensing signal through Eqs. (2)-(4). We also apply a radius selection and only use voids within range $17 < R_V < 25 \text{ Mpc/h}$, as small voids have been shown to trace overdense regions [82] and larger voids suffer from much lower number densities (Appendix B). The total number density of the selected voids is approximately $4.7 \times 10^{-4} \text{ Mpc}^{-3} h^3$, with slight variations among different cosmologies (Fig. 11).

C. Ray-tracing Mocks

To further investigate the observational effects, as well as validate the theoretical modelling of void lensing signal described in Section II, we generate mock shear catalogues following the multiplane ray-tracing method introduced in Ref. [83]. To simplify the analysis, we place all source galaxies at $z_s = 0.75$ and run ray-tracing up to this redshift with an angular resolution $\sim 0.8 \text{ arcmin}$. The lensing efficiency for $z_s = 0.75$ peaks around $z_l = 0.3$, which is consistent with our foreground galaxy and void catalogues (Section III B 1). Following Ref. [83], we adopt the flat-sky approximation, which should not bias our results given that we only focus on scales smaller than 50 Mpc/h (twice the maximum radius of our selected void samples).

Limited by the boxsize, it is unable to ray-trace to $z = 0.75$ in a single simulation box. One possible solution is to replicate boxes to increase the volume (e.g. Ref [40]), but may suffer from artificial repetition of structures (see Ref. [84], who also explore the strategies to minimize this impact by optimizing the line-of-sight selection). Ref. [85] proposed an alternative remapping method to transform a cubic box into a rectangular cuboid, with preserving the continuity and avoiding the repetition of structures. We refer to this method to generate a suite of density slices with a thickness of $L \approx 125 \text{ Mpc/h}$ for ray-tracing (except for the first and last slices, see Appendix C for more details). The redshift evolution of structures is incorporated by using snapshots saved with $\Delta z = 0.05$. As the dark matter and neutrino components are realized in different ways in the simulations, we smooth the dark matter particles with a CIC kernel and also resample the original neutrino overdensity mesh to

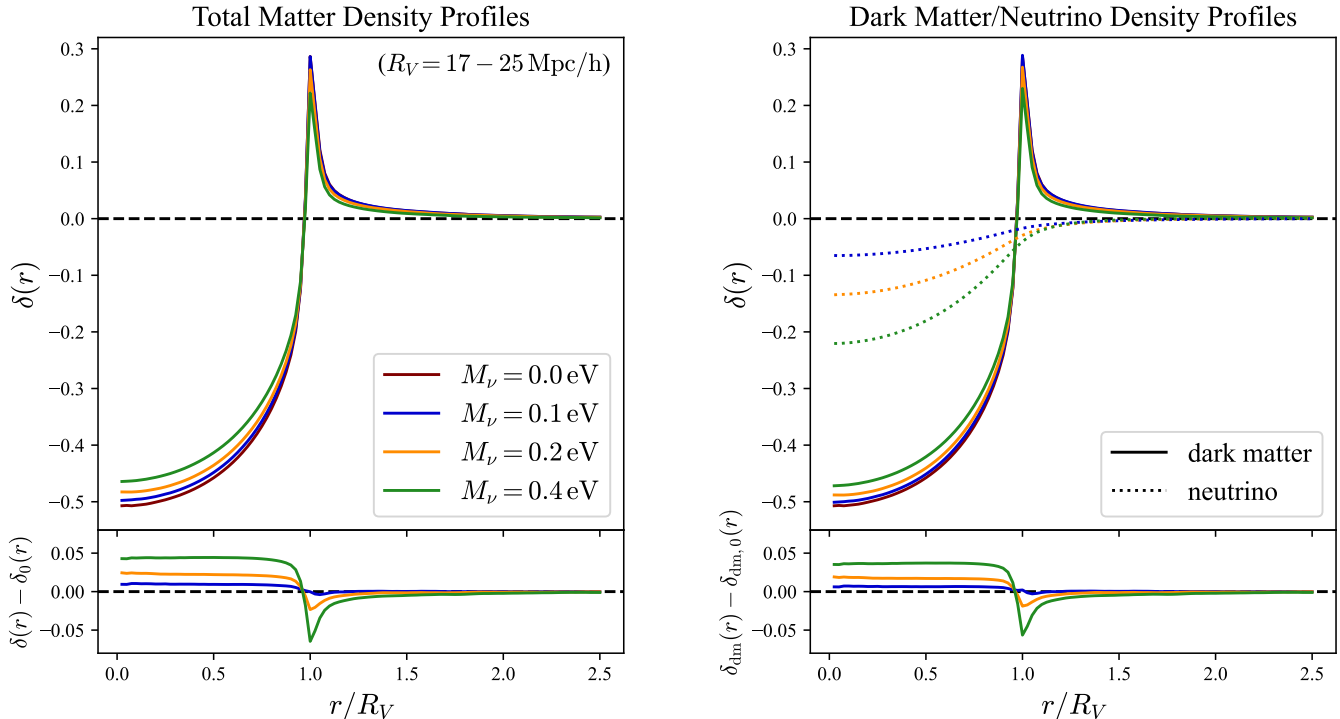


FIG. 3. Combined density profiles of voids with $17 < R_V < 25 \text{ Mpc/h}$ measured in simulations. Different colors represent simulations with different neutrino masses. The left panel shows the total density profile, while the right panel presents dark matter and neutrino components separately with solid and dotted lines. The bottom panels display the differences between simulations with massive neutrinos and massless neutrinos ($\delta_0(r)$).

get the total matter distribution in each slice.

With the ray-tracing results at $z = 0.75$, we randomly sample source galaxy catalogues with a number density $10/\text{arcmin}^2$, which lies between the typical values of stage-III surveys [86, 87] and stage-IV predictions [88, 89]. The shear values of each source are linearly interpolated from ray-tracing results. We further incorporate a Gaussian random shape noise with $\sigma_e = 0.3$ to mock real observations.

To obtain the consistent foreground void catalogues, we first remap galaxies in simulation box to a slice using the same method, and subsequently identify voids with the remapped galaxy positions. Since the periodic boundary conditions are partially broken by the remapping, we drop voids with centers outside the slice. The slice thickness 125 Mpc/h corresponds to a redshift width $\delta z \approx 0.05$ at $z_l = 0.3$, which is actually narrower than the typical redshift bins adopted in galaxy-galaxy lensing studies.

In addition, the transverse extent of the remapped slices allows for a split into 15 subregions with an angular area of 8400 deg^2 at $z = 0.3$ (see Appendix C), which are used as multiple independent realizations for the covariance estimation in Section V B. Fig. 2 shows the shear auto-correlation functions, ξ_+ and ξ_- , of our mock source catalogues averaged over all 15 sub-regions, demonstrating a good agreement between ray-tracing results and

the prediction of 3D matter power spectrum. Finally, we note that, as a compromise for the limited simulation data, the flat-sky approximation and remapping method adopted in generating mocks may lead to slight inaccuracies in the covariance estimation. Given that we only focus on the cross-correlation in this work, and the covariance is dominated by the shape noise (Fig. 7), we do not expect these effects would bias our conclusions and dedicate more accurate shear mocks to future work.

IV. VOID STATISTICS

In this section, we present the measurement of void density profile (Section IV A) and void lensing signals (Section IV B) from the simulation and mock data. We also compare the theoretical model of $\Delta\Sigma$ and measurements from mocks in Section IV B. It is noted that the results shown in this section are the average of all voids with radius $17 < R < 25 \text{ Mpc/h}$ (see Section III B 2), which is also used for the cosmological inference in next section. We present the results in separate radius bins in Appendix A.

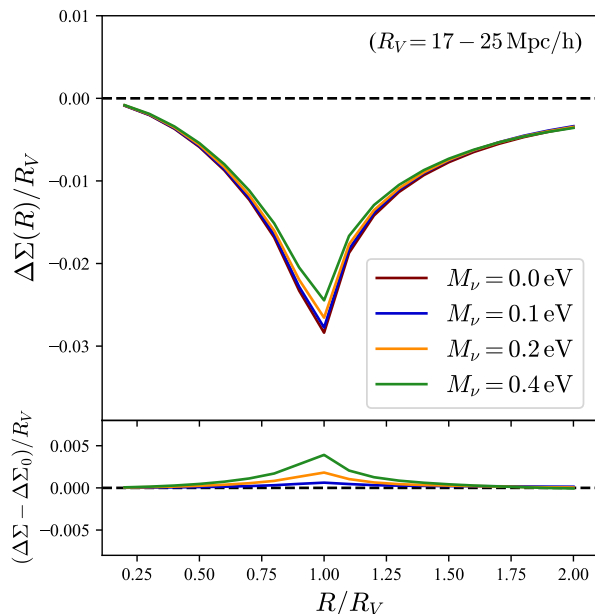


FIG. 4. Theoretical model of the combined void lensing signal $\Delta\Sigma$ for voids with $17 < R < 25$ Mpc/h. Different colors indicate different neutrino masses. The bottom panel shows the differences between results of massive neutrinos and the massless case.

A. Void Density Profile $\delta(r)$

Fig. 3 shows the void density profiles measured in the $z = 0.3$ snapshot of simulations with different neutrino masses. The results are estimated from the complete void catalogue within the simulation box, and exhibit negligible jackknife errors, with an average S/N ratio of order 10^3 , owing to the high number density of DT voids.

The results demonstrate that the selected DT voids trace underdense regions with the negative central density contrast. The left panel of Fig. 3 shows the total matter distribution. For DT voids, they always present a sharp density peak at boundary ($r = R_V$), which is distinguishable from other voids, such as the universal profile [35] for voids identified with modified ZOBOV, which have much smoother density walls at boundary. The underlying reason for this feature is that, by definition, there are always four galaxies located at void boundary. As galaxies typically reside in high-density regions, this results in a significant density increase. At larger radial distance, the density returns to homogeneity ($\delta = 0$) when averaging over a large sample of voids.

Similar to the results in Ref. [26], for DT voids, massive neutrinos also induce a higher density at central underdense regions and a lower density peak at boundary, and the changes increase with neutrino mass. To further demonstrate this phenomenon, we show the separate distribution of neutrinos and dark matter in the right panel of Fig. 3, which indicates that neutrinos generally follow the underlying dark matter distribution through gravi-

tational attraction, but are much less clustered. Meanwhile, the gravitational influence of neutrinos also suppresses the clustering of dark matter. This is a consequence of the large thermal velocities of neutrinos, which prevent them from efficiently collapsing into dark matter potential wells. The balance between neutrino velocity dispersion and gravitational effect changes with neutrino mass. On the one hand, the overall gravitational effect of neutrinos increases with neutrino mass, making massive neutrinos have a higher impact on dark matter distribution. On the other hand, a higher neutrino mass corresponds to a lower velocity, making neutrinos easier to collapse. The competition between these two effects comprises the sensitivity of void density profile to neutrino mass, as shown in Fig. 3.

B. Void Lensing Signal $\Delta\Sigma(R)$

As stated in Section II, the differences in void density profiles leave imprints on the weak lensing signal. Following Eqs (2) and (4), we theoretically model the weak lensing signal $\Delta\Sigma$ of voids from the measured 3D density profiles of total matter (both dark matter and neutrinos) presented in Section IV A. The results are shown in Fig. 4. Due to the positive density slope at the interior of voids, $\Delta\Sigma(R)$ shows a minimum around the void boundary, which is consistent with previous void lensing studies and measurements from observational data [53, 59]. Similar to Fig. 3, the statistical errors of $\Delta\Sigma$ are invisible as well (S/N ratio $\sim 10^3$) due to the large number of voids included in the calculation. The comparison between different neutrino masses shows that more massive neutrinos result in a less prominent void lensing signal (i.e. a higher $\Delta\Sigma(R)$ for large voids), consistent with the fact that nonzero neutrino mass results in more homogeneous matter distribution.

To validate the theoretical model shown in Fig. 4, we also measure the void lensing signals in the ray-tracing mocks presented in Section III C. The measurements are conducted in adaptive radius bins with resolution $0.1 R_V$ for voids with different sizes. To simplify the analysis, we only consider the cross-correlation between two single redshift bins, and place all mock source galaxies at $z_s = 0.75$. We investigate the cases both without and with shape noise ($\sigma_e = 0.3$), with a source number density $10/\text{arcmin}^2$.

Fig. 5 shows the measurements with theoretical models overlaid. For readability, here we only plot results for $M_\nu = 0.0$ and 0.4 eV. The errorbars of the data points are from the diagonal terms of the covariance matrix, the estimate of which is presented in Section V B. A clear alignment between theoretical model and measurement from mock data can be found in the left panel, which is free of shape noise. With shape noise included, the lensing signals still follow the models well, although the errors increase significantly. The difference in $\Delta\Sigma$ between $M_\nu = 0.0$ and 0.4 eV reaches $\sim 1\sigma$ level in the

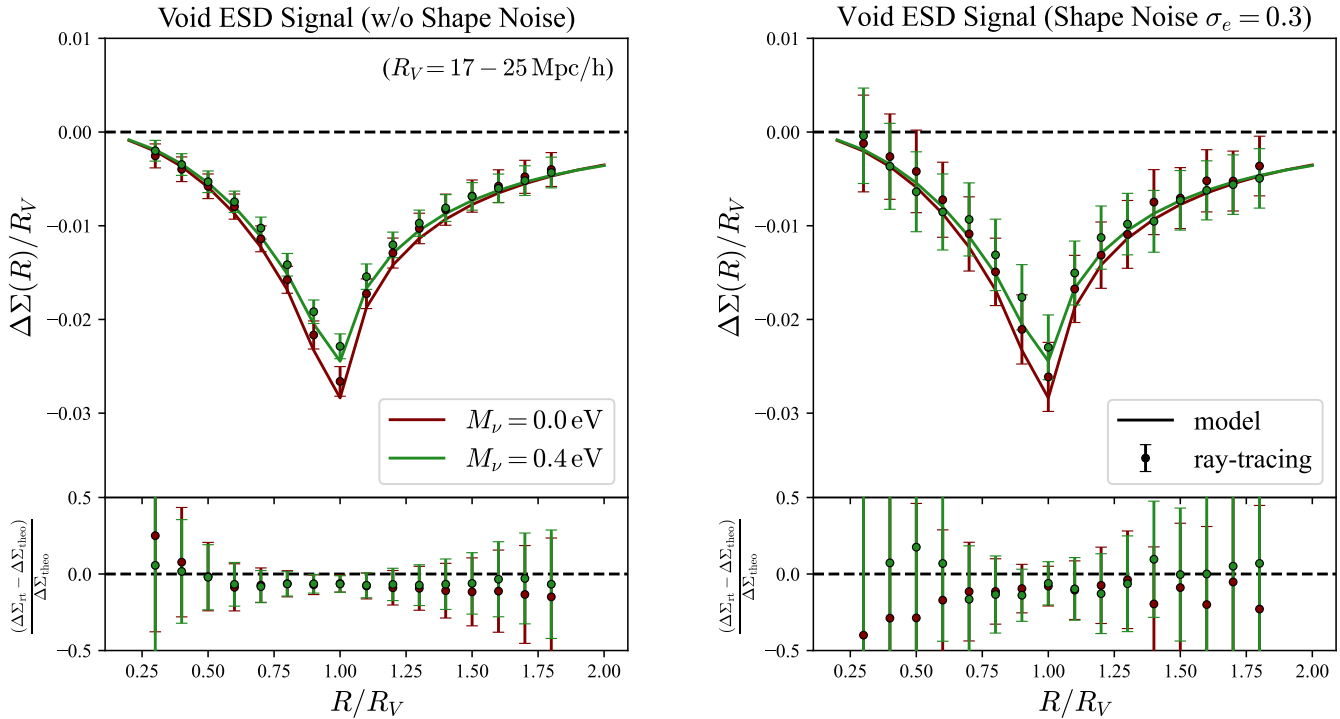


FIG. 5. Comparison between void lensing signal measured in ray-tracing mocks (data points) and theoretical models (solid lines). The radius ranges of measurement are $0.3 \leq R/R_V \leq 1.8$ with a bin size $\Delta R = 0.1 R_V$. Different colors indicate the measurements in simulations with $M_\nu = 0.0 \text{ eV}$ (red) and $M_\nu = 0.4 \text{ eV}$ (green). The left panel shows the measurements from mock source catalogues without shape noise, while the right panels display the results including shape noise $\sigma_e = 0.3$. The errorbars are estimated with 15 realizations in Section V B. Two bottom panels show the differences between the mock measurements ($\Delta\Sigma_{\text{rt}}$) and models ($\Delta\Sigma_{\text{theo}}$).

vicinity of void boundary, in the case with shape noise, which indicates a potential constraint on neutrino mass from void lensing effect. We further investigate the constraining power in the next section.

V. CONSTRAIN NEUTRINO MASS WITH VOID LENSING SIGNAL

As the comparison in Section IV B validates the modelling of $\Delta\Sigma$ from void density profile, in this section, we further investigate the constraint on neutrino mass based on the theoretical models. We present the data vector and linear fitting of $\Delta\Sigma - M_\nu$ in Section V A, and the estimate of covariance matrix in Section V B. Finally we conclude with the sampling of posterior and discussions (Section V C).

A. Data and Model

Fig. 4 shows that the differences in void lensing signal exist at all radii but become more prominent around void boundary. Therefore, we use data points at $0.3 \leq R/R_V \leq 1.4$ for the following analysis. Here we re-bin

the theoretical $\Delta\Sigma(R)$ model into radius bins with an interval $R = 0.1 R_V$, which is same as the resolution of the measurements in ray-tracing mocks. We then follow Ref. [40] to combine all voids with weight $1/R_V$ and present void lensing signal as $\Delta\Sigma/R_V$ (we omit R_V in the remaining text) in Figs. 4 and 5. The investigation of other weights to optimize the S/N ratio of the measurement is out of the scope of this work, and we dedicate it to future work.

From the data vectors of different neutrino masses, we find that the relation between $\Delta\Sigma(R)$ and M_ν can be well fitted by linear functions, with slopes changing with radius R . We show the fitting at three different radii $R/R_V = 0.6, 1.0, 1.2$ in Fig. 6, and have checked the linear relation always persists in the radius range we use for inference. We note that the errorbars become invisible in the plot, as the jackknife errors for theoretical $\Delta\Sigma(R)$ model used here are extremely small (see Section IV A), but we take the errors into account when doing the fitting. We then use the suite of best-fit linear relations at different radii as the model in the likelihood.

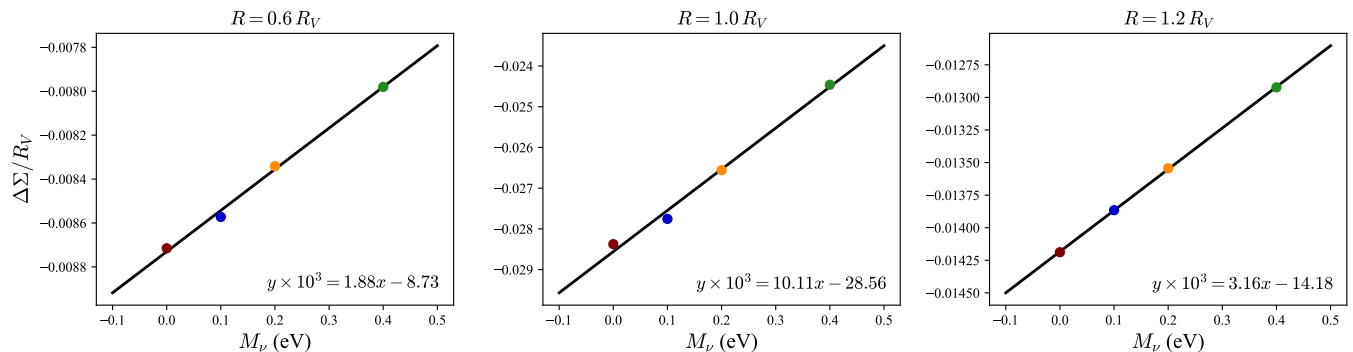


FIG. 6. Linear fitting of the relation between $\Delta\Sigma$ and M_ν at three different radii. The colors of data points are consistent with Fig. 3 and Fig. 4. The jackknife errorbars of data points are too small to be visible. The functions in each panel present the best-fit linear relations at different radii.

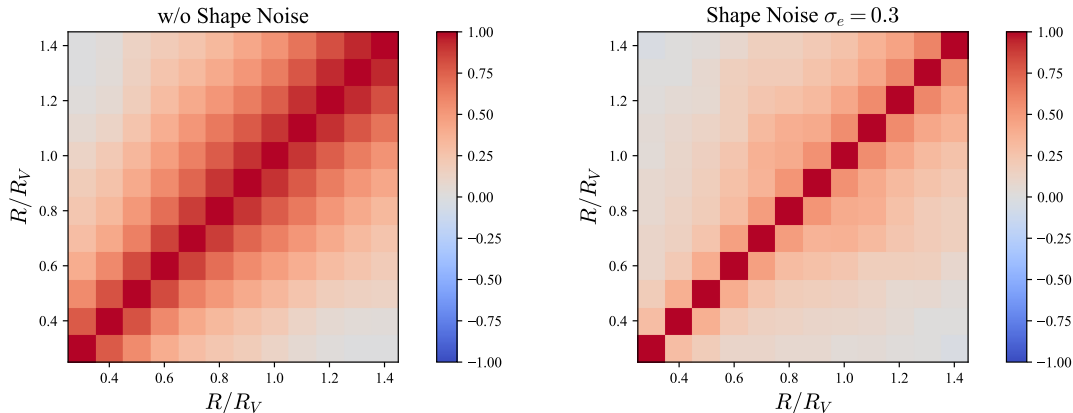


FIG. 7. Correlation matrix estimated with 15 realizations. The matrix is obtained by normalizing the covariance matrix with its diagonal elements. The two panels display results without (left) and with (right) shape noise.

B. Covariance Matrix

Besides the model discussed in Section V A, covariance is also necessary for inference. Limited by the number of simulations, we cannot follow the standard way to estimate covariance from a suite of simulations with different initial conditions. Therefore, we generate 15 realizations of ray-tracing mocks using box-remapping described in Section III C and follow the method presented in to derive the covariance matrix. Ref. [90] proposed an effective method to improve the covariance estimation from a limited number of realizations by combining jackknife resamplings in each realization, which can attain the same accuracy as using ~ 7 times more realizations. The estimator \bar{C}_{ij} presents as

$$\bar{C}_{ij} = \frac{1}{N_M} \sum_{m=1}^{N_M} \hat{C}_{ij}^{(m)}, \quad (8)$$

$$\hat{C}_{ij} = \frac{N_{JK} - 1}{N_{JK}} \sum_{k=1}^{N_{JK}} (y_i^k - \bar{y}_i)(y_j^k - \bar{y}_j); \quad (9)$$

where N_{JK} is the number of jackknife subsamples in each realization and N_M is the total number of realizations used. \bar{y}_i is the data vector average over all jackknife replica in each realization. In this work, we adopt $N_M = 15$ and $N_{JK} = 64$. The correlation matrices obtained from normalizing the covariance matrix with diagonal terms are presented in Fig. 7, which are smooth and show marked correlations between neighboring bins.

It is noted that, as stated in Section III C, we apply several approximations when generating ray-tracing mocks. For instance, to utilize the entire slice cross-section at $z = 0.3$, it is required to complement the slices at $z > 0.3$ through the periodic boundary condition, which results in the repetition of path structures at $z > 0.3$ in different realizations. In addition, each slice originates from the entire box of different snapshots in the same simulation, which also leads to the appearance of similar structures in different slices. Both of these approximate operations may lead to slightly inaccuracies in covariance. However, as shown in Fig. 7, the covariance gets dominated by shape noise when taking it into account. Due to the fact that the constraint on neutrino mass given by void lens-

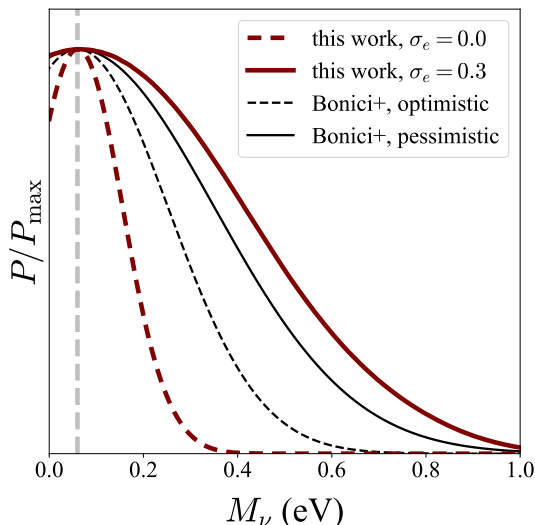


FIG. 8. Posteriors of neutrino mass in the cases without (red dashed line) and with (red solid line) shape noise. The vertical gray dashed line indicates the fiducial value $M_\nu = 0.06$ eV. As a comparison, the black lines show the optimistic and pessimistic forecast results of Ref. [91] (see the Table 5 therein), which utilizes the large-scale cross-correlation between voids and shear catalogues and differs from our method. These two approaches are complementary and can be combined to yield improved constraints.

ing is still quite loose (Section V C), we do not expect that these limitations would bias our final results significantly, and leave more careful covariance estimation to future work.

C. Posterior on M_ν

With the linear model and covariance described above, we sample the posterior of neutrino mass with ULTRANEST [92], assuming a Gaussian likelihood and a fiducial cosmology with neutrino mass $M_\nu = 0.06$ eV. The posteriors are shown in Fig. 8 with a truncation to $M_\nu > 0$. With our setup (see Section III C), the void lensing effect can independently provide a constraint on neutrino mass as $\sigma(M_\nu) = 0.096$ eV in the absence of shape noise, and it becomes $\sigma(M_\nu) = 0.340$ eV when including a $\sigma_e = 0.3$ shape noise.

Ref. [91] also investigated the cross-correlation between voids and weak lensing and presented forecasts for the *Euclid* survey with the same shape noise level $\sigma_e = 0.3$. However, their analyses only used cross-correlation at large scale to avoid explicit modelling of void density profile, which is actually complementary to our method. For comparison, we also plot their forecast results in Fig. 8. Their studies combine the auto-clustering of weak lensing shear and voids and the cross-correlation, and eventually present a constraint as $\sigma(M_\nu) = 0.193$ eV (0.292 eV) in the optimistic (pessimistic) case, which is in the similar

constraining level to our results.

It should be noted that our current result is limited to only one parameter M_ν , while Ref. [91] constrain multiple cosmological parameters simultaneously. However, as stated in Ref. [26], void lensing would potentially help break the degeneracy between neutrino mass and other cosmological parameters, such as Ω_m and σ_8 . Therefore, we anticipate a tighter cosmological constraint from the synergy between void lensing and other statistics, such as galaxy lensing ‘ $3 \times 2pt$ ’. In addition, tomographic analyses combining voids across multiple redshift bins adopted in Ref.[91] also help to improve the constraining power. These extensions merit further investigation in future work.

VI. DISCUSSIONS AND SUMMARY

Massive neutrinos leave distinct imprints on both the cosmic expansion history and evolution of LSS, providing important opportunities to constrain their total mass with cosmological observations [10]. As the underdense regions in the Universe, cosmic voids offer essential environments for investigating neutrino properties [26].

In this work, we investigate the constraining power of weak lensing effect of cosmic voids on neutrino mass, using realistic mocks generated from N -body simulation with varying total neutrino masses (0 eV, 0.1 eV, 0.2 eV and 0.4 eV). For the void catalogues, we fit an HOD model to BOSS LOWZ galaxies in $0.2 < z < 0.4$, identify DT voids with the DIVE void finder developed by Ref. [64] and select voids with $17 < R_V < 25$ Mpc/h. The weak lensing shear catalogues are generated through multiplane ray-tracing simulations [83]. In addition, for the sake of future cosmological applications, we validate the forward theoretical modelling of lensing signal from the void density profile.

Our main findings are summarized as follows:

1. The density profiles of DT voids show clear sensitivity to the total neutrino mass M_ν . The presence of massive neutrinos leads to higher void interior densities and reduced density peaks at the void boundary (Fig. 3). These effects become more prominent as with neutrino mass increasing.
2. Variations of void density profiles leave observable imprints in the weak lensing signal. For voids of the same size, massive neutrinos result in a less pronounced lensing signal (Fig. 4). In particular, the excess surface density profile, $\Delta\Sigma(R)$, exhibits a clear linear dependence on the neutrino mass within $R < 1.4 R_V$ (Fig. 6).
3. The weak lensing signal of DT voids yields an independent constraint on the total neutrino mass of $\sigma(M_\nu) = 0.096$ eV, in the absence of shape noise, and $\sigma(M_\nu) = 0.340$ eV when including realistic

galaxy shape noise with $\sigma_e = 0.3$. These constraints are comparable to those obtained in other weak lensing studies.

4. The void density profile provides an effective approach for modelling the void lensing signal, as validated across different cosmologies (Fig. 4) and void size bins (Appendix A). This alleviates the need for full ray-tracing simulations and facilitates the development of emulator-based models for void lensing in future work.

Looking ahead, there are several aspects to be investigated in future works. Firstly, a more delicate modelling of the void lensing signal and accurate estimation of the covariance are required for future applications to observational data. Ref. [93] investigated the simulation-based inference (SBI) for void lensing modelling, while emulator-based approaches have also significantly facilitated cosmological analyses (e.g. Refs. [94, 95]). This also necessitates higher-fidelity mocks that incorporate more observational effects beyond the shape noise, such as imaging systematics, magnification bias and intrinsic alignments [96]. Moreover, voids identified in redshift space are known to show properties distinct from those in real space [97, 98], which also merits more detailed investigations.

In addition, analogous to galaxy-galaxy lensing, tomographic analyses of void lensing have the potential to enhance the constraining power, owing to both the redshift evolution of void properties and the increased void sample size [91]. Furthermore, combining void lensing with other probes, such as void clustering, void size function and other weak lensing probes including the standard ‘3x2pt’ analysis, can break parameter degeneracies and yield tighter cosmological constraints. These synergies also facilitate our future extensions of this framework to more cosmological parameters beyond M_ν .

In conclusion, our investigations based on mock data demonstrate that void lensing effect provides an effective and complementary probe for constraining neutrino mass with cosmological surveys. We anticipate that void lensing will help promote the cosmological constraints in existing cosmological surveys, including DESI, *Euclid* [99], KiDs, DES, HSC, as well as future programs, such as MUST [100], CSST [101] and LSST [102].

ACKNOWLEDGMENTS

We would like to thank Qiao Wang for helpful discussions on the ray-tracing code. WSX appreciates the insightful discussions with Siyi Zhao and Eric Jullo. We acknowledge the support from National Key R&D Program of China (Grant No. 2023YFA1605600) and National Natural Science Foundation of China (Grant No. 12303005). YL acknowledges the support from Shuimu Tsinghua Scholar Program (No. 2022SM173) and Swiss

National Science Foundation research grant ‘‘Cosmology with 3D Maps of the Universe’’ (No. 200020_207379).

WSX acknowledges the Tsinghua Astrophysics High-Performance Computing platform for providing computational and data storage resources that have contributed to the research results within this paper.

In this work, we also use the following python packages in addition to those already cited in the main content: ASTROPY [103], NUMPY [104], MATPLOTLIB [105], SCIPY [106] and GETDIST [107].

Appendix A: Void Lensing Signal in Different Radius Bins

Figs. 9 and 10 present the measurements of void lensing signal $\Delta\Sigma(R)$ in different radius bins, along with the corresponding theoretical models derived from void density profiles, in the simulation with $M_\nu = 0.0\text{ eV}$. We find great agreements between models and measurements across all radius bins, which further validate the modelling method. The errorbars increase for larger voids, owing to the much lower number density of voids with large radius.

The results in other cosmologies are similar, and the trend of a weaker void lensing signal with increasing neutrino mass persists in all radius bins.

Appendix B: Void Size Function

We present the void size function (VSF) measured in simulations with different neutrino masses in Fig. 11. The results demonstrate the sensitivity of the VSF to neutrino mass, which results in an excess of small voids and a reduced amount of large voids with the existence of massive neutrinos. Our results are consistent with Ref. [26], but show a lower statistical significance. We attribute this to the potential correlation between the VSF of DT voids and galaxy clustering, as we control the 2-point clustering of our galaxy samples with HOD fitting.

Appendix C: Ray-tracing Slices from Box Remapping

Following Ref. [85], for a simulation box with periodic boundary conditions, the cuboid remapping method can transform a cubic box to a rectangular cuboid with preserving the continuity and avoiding repetition of structures. In this work, we adopt the method on the x - z plane to transform our simulation box of side length $L = 1500\text{ Mpc/h}$ into a cuboid of $(1500\sqrt{8^2 + 9^2}, 1500, 1500/\sqrt{8^2 + 9^2})\text{ Mpc/h}$ (see Fig.2 in Ref. [85] for an illustration). We construct the ray-tracing lightcones by stacking a sequence of remapped boxes up to $z_s = 0.75$ along their shortest side.

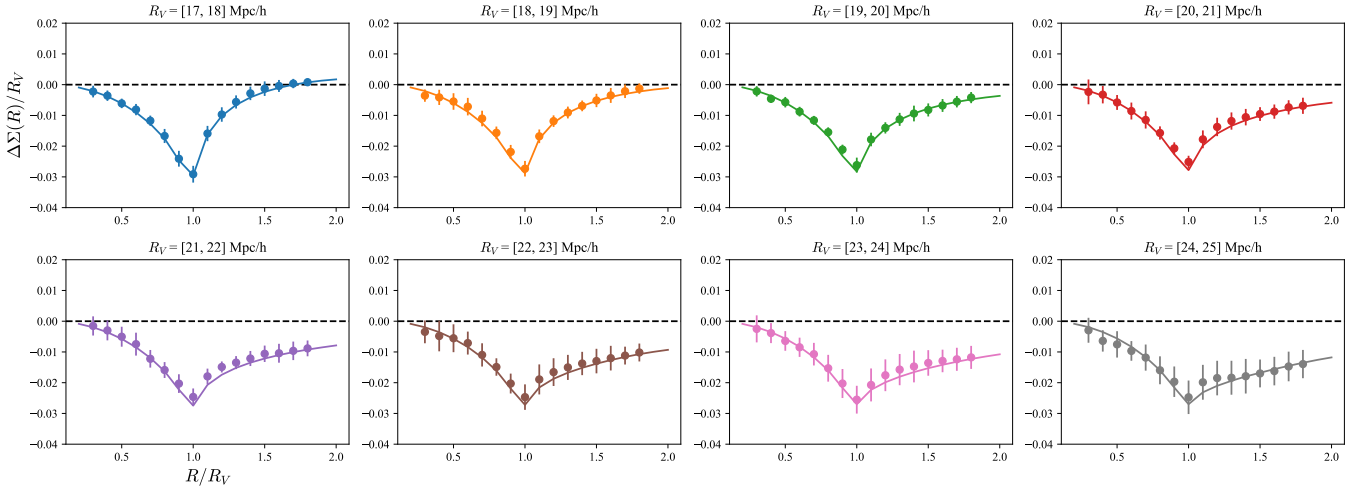


FIG. 9. Comparison between the theoretical models of void lensing signal $\Delta\Sigma$ (solid lines) and measurements from ray-tracing mocks (data points) in different radius bins. The results shown here are from the massless-neutrino cosmology.

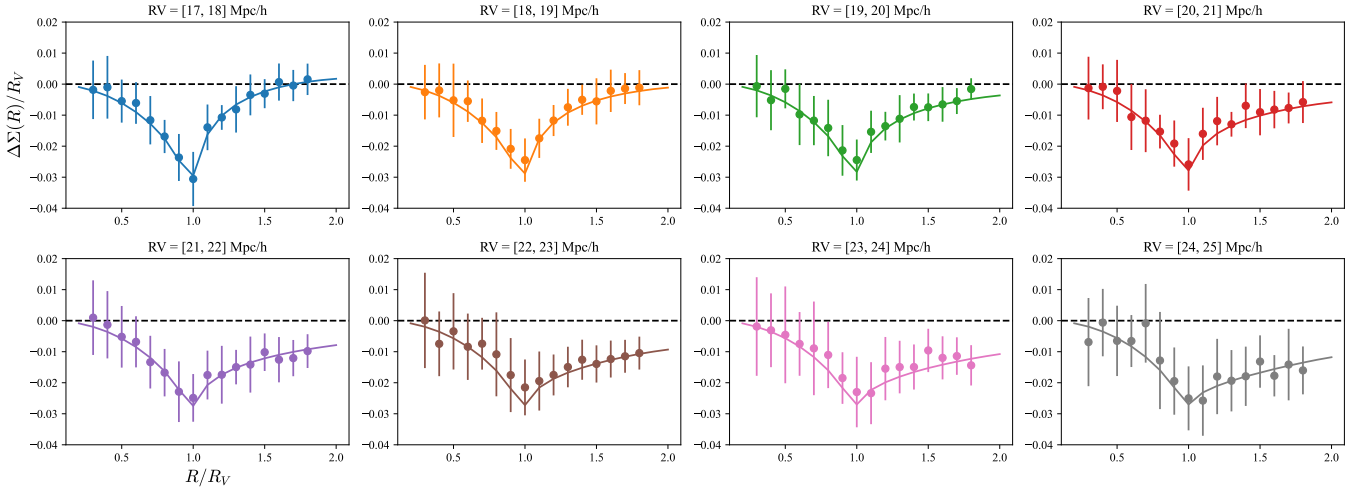


FIG. 10. Same as Fig. 9, with shape noise $\sigma_e = 0.3$ included.

This results a suite of lensing ‘slices’ with thickness of $1500/\sqrt{8^2 + 9^2} \approx 125 \text{ Mpc/h}$ (except for the first and last slices), which is close to the safe range presented in Ref. [108]. Each single slice therefore comes from a full remapped box, while the inside structures are taken from the closest simulation snapshots.

In the analysis, we only use voids at $z_l = 0.3$ for the void lensing cross-correlation. For this purpose, we make use of the full remapped slice at $z_l = 0.3$, which allows for a split into 15 subregions, each covering 8400 arcmin^2 . As there is no structure repetition within each remapped slice, the same void does not appear multiple times in different subregions.

However, the ray-tracing algorithm requires all slices to subtend at least the same angular area. For slices at $z > 0.3$, the corresponding physical area therefore exceeds a single remapped slice. We complement these additional areas using the periodic boundary conditions in the two transverse dimensions, which are preserved by the remapping method.

This procedure actually leads to the repetition of the same line-of-sight structures across the 15 subregions, and may affect the covariance estimation [109]. Nevertheless, this would not bias our results, as the covariance will be dominated by galaxy shape noise as shown in Section VB.

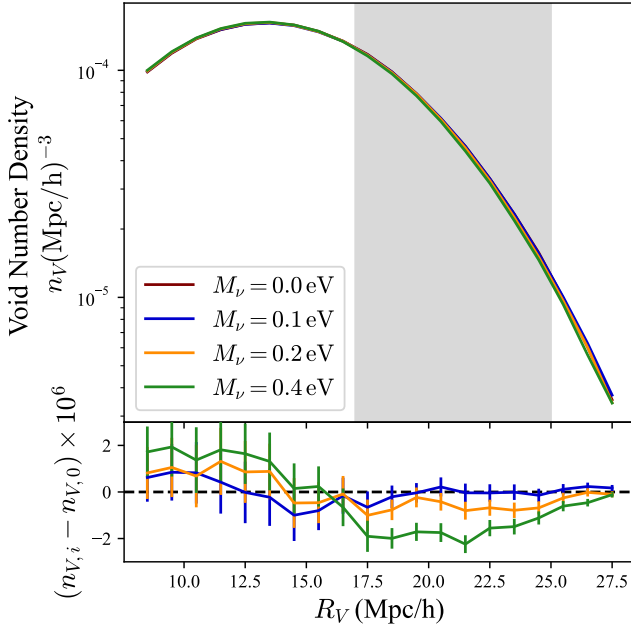


FIG. 11. Void size function measured in simulations with different neutrino masses. The radius bin used here is $\Delta R_V = 1$ Mpc/h. The shaded region in the upper panel indicates the void radius range that we use in this work. The bottom panel displays the differences between results of massive neutrinos and the massless-neutrino case.

[2] M. S. Madhavacheril, F. J. Qu, B. D. Sherwin, N. MacCrann, Y. Li, I. Abril-Cabezas, P. A. R. Ade, S. Aiola, T. Alford, M. Amiri, *et al.*, *ApJ* **962**, 113 (2024), arXiv:2304.05203 [astro-ph.CO].

[3] Z. Pan, F. Bianchini, W. L. K. Wu, P. A. R. Ade, Z. Ahmed, E. Anderes, A. J. Anderson, B. Ansarinejad, M. Archipley, K. Aylor, *et al.*, *Phys. Rev. D* **108**, 122005 (2023), arXiv:2308.11608 [astro-ph.CO].

[4] E. Abdalla, G. F. Abellán, A. Aboubrahim, A. Agnello, Ö. Akarsu, Y. Akrami, G. Alestas, D. Aloni, L. Amendola, L. A. Anchordoqui, *et al.*, *Journal of High Energy Astrophysics* **34**, 49 (2022), arXiv:2203.06142 [astro-ph.CO].

[5] K. Lodha, R. Calderon, W. L. Matthewson, A. Shafieloo, M. Ishak, J. Pan, C. Garcia-Quintero, D. Huterer, G. Valogiannis, L. A. Ureña-López, *et al.*, *Phys. Rev. D* **112**, 083511 (2025), arXiv:2503.14743 [astro-ph.CO].

[6] M. Ishak, J. Pan, R. Calderon, K. Lodha, G. Valogiannis, A. Aviles, G. Niz, L. Yi, C. Zheng, C. Garcia-Quintero, *et al.*, *J. Cosmology Astropart. Phys.* **2025**, 053 (2025), arXiv:2411.12026 [astro-ph.CO].

[7] E. Chaussidon, C. Yèche, A. de Mattia, C. Payterne, P. McDonald, A. J. Ross, S. Ahlen, D. Bianchi, D. Brooks, E. Burtin, *et al.*, *J. Cosmology Astropart. Phys.* **2025**, 029 (2025), arXiv:2411.17623 [astro-ph.CO].

[8] W. Elbers, A. Aviles, H. E. Noriega, D. Chebat, A. Menegas, C. S. Frenk, C. Garcia-Quintero, D. Gonzalez, M. Ishak, O. Lahav, *et al.*, *Phys. Rev. D* **112**, 083513 (2025), arXiv:2503.14744 [astro-ph.CO].

[9] Katrin Collaboration, M. Aker, D. Batzler, A. Beglarian, J. Behrens, J. Beisenkötter, M. Biassoni, B. Bieringer, Y. Biondi, F. Block, *et al.*, *Science* **388**, 180 (2025), arXiv:2406.13516 [nucl-ex].

[10] S. Navas, C. Amsler, T. Gutsche, C. Hanhart, J. J. Hernández-Rey, C. Lourenço, A. Masoni, M. Mikhasenko, R. E. Mitchell, C. Patrignani, *et al.*, *Phys. Rev. D* **110**, 030001 (2024).

[11] S. Vagnozzi, E. Giusarma, O. Mena, K. Freese, M. Gerbino, S. Ho, and M. Lattanzi, *Phys. Rev. D* **96**, 123503 (2017), arXiv:1701.08172 [astro-ph.CO].

[12] S. R. Choudhury and S. Hannestad, *J. Cosmology Astropart. Phys.* **2020**, 037 (2020), arXiv:1907.12598 [astro-ph.CO].

[13] S. Brieden, H. Gil-Marín, and L. Verde, *J. Cosmology Astropart. Phys.* **2022**, 024 (2022), arXiv:2204.11868 [astro-ph.CO].

[14] DESI Collaboration *et al.*, *Phys. Rev. D* **112**, 083515 (2025), arXiv:2503.14738 [astro-ph.CO].

[15] W. Elbers, C. S. Frenk, A. Jenkins, B. Li, and S. Pascoli, *Phys. Rev. D* **111**, 063534 (2025), arXiv:2407.10965 [astro-ph.CO].

[16] W. Hu, D. J. Eisenstein, and M. Tegmark, *Phys. Rev. Lett.* **80**, 5255 (1998), arXiv:astro-ph/9712057 [astro-ph].

[17] K. N. Abazajian and M. Kaplinghat, *Annual Review of Nuclear and Particle Science* **66**, 401 (2016).

[18] DESI Collaboration *et al.*, *J. Cosmology Astropart. Phys.* **2025**, 028 (2025), arXiv:2411.12022 [astro-ph.CO].

[19] R. de Belsunce and L. Senatore, *J. Cosmology Astropart. Phys.* **2019**, 038 (2019), arXiv:1804.06849 [astro-ph.CO].

[20] F. Kamalinejad and Z. Slepian, arXiv e-prints, arXiv:2011.00899 (2020), arXiv:2011.00899 [astro-ph.CO].

[21] Y. Liu, Y. Yu, H.-R. Yu, and P. Zhang, *Phys. Rev. D* **101**, 063515 (2020), arXiv:2002.08846 [astro-ph.CO].

[22] W. Liu, A. Jiang, and W. Fang, *J. Cosmology Astropart. Phys.* **2023**, 037 (2023), arXiv:2302.08162 [astro-ph.CO].

[23] J. H. T. Yip, M. Biagetti, A. Cole, K. Viswanathan, and G. Shiu, *J. Cosmology Astropart. Phys.* **2024**, 034 (2024), arXiv:2403.13985 [astro-ph.CO].

[24] M. H. Jalali Kanafi, S. Ansarifard, and S. M. S. Movahed, *MNRAS* **535**, 657 (2024), arXiv:2311.13520 [astro-ph.CO].

[25] J. Li and C. Zhao, arXiv e-prints, arXiv:2512.07236 (2025), arXiv:2512.07236 [astro-ph.CO].

[26] E. Massara, F. Villaescusa-Navarro, M. Viel, and P. M. Sutter, *J. Cosmology Astropart. Phys.* **2015**, 018 (2015), arXiv:1506.03088 [astro-ph.CO].

[27] P. Vielzeuf, M. Calabrese, C. Carbone, G. Fabbian, and C. Baccigalupi, *J. Cosmology Astropart. Phys.* **2023**, 010 (2023), arXiv:2303.10048 [astro-ph.CO].

[28] L. Thiele, E. Massara, A. Pisani, C. Hahn, D. N. Spergel, S. Ho, and B. Wandelt, *ApJ* **969**, 89 (2024), arXiv:2307.07555 [astro-ph.CO].

[29] M. Jöeveer, J. Einasto, and E. Tago, *MNRAS* **185**, 357 (1978).

[30] S. A. Gregory and L. A. Thompson, *ApJ* **222**, 784 (1978).

[31] P. M. Sutter, G. Lavaux, B. D. Wandelt, and D. H. Weinberg, *ApJ* **761**, 44 (2012), arXiv:1207.2524 [astro-ph.CO].

- ph.CO].
- [32] D. C. Pan, M. S. Vogeley, F. Hoyle, Y.-Y. Choi, and C. Park, *MNRAS* **421**, 926 (2012), arXiv:1103.4156 [astro-ph.CO].
- [33] N. I. Libeskind, R. van de Weygaert, M. Cautun, B. Falck, E. Tempel, T. Abel, M. Alpaslan, M. A. Aragón-Calvo, J. E. Forero-Romero, R. Gonzalez, *et al.*, *MNRAS* **473**, 1195 (2018), arXiv:1705.03021 [astro-ph.CO].
- [34] K. A. Douglass, D. Veyrat, and S. BenZvi, *ApJS* **265**, 7 (2023), arXiv:2202.01226 [astro-ph.GA].
- [35] N. Hamaus, P. M. Sutter, and B. D. Wandelt, *Phys. Rev. Lett.* **112**, 251302 (2014), arXiv:1403.5499 [astro-ph.CO].
- [36] E. Paillas, C. D. P. Lagos, N. Padilla, P. Tissera, J. Helly, and M. Schaller, *MNRAS* **470**, 4434 (2017), arXiv:1609.00101 [astro-ph.CO].
- [37] A. Pisani, P. M. Sutter, N. Hamaus, E. Alizadeh, R. Biswas, B. D. Wandelt, and C. M. Hirata, *Phys. Rev. D* **92**, 083531 (2015), arXiv:1503.07690 [astro-ph.CO].
- [38] C. Zhao, A. Variu, M. He, D. Forero-Sánchez, A. Tamone, C.-H. Chuang, F.-S. Kitaura, C. Tao, J. Yu, J.-P. Kneib, *et al.*, *MNRAS* **511**, 5492 (2022), arXiv:2110.03824 [astro-ph.CO].
- [39] E. L. D. Perico, R. Voivodic, M. Lima, and D. F. Mota, arXiv e-prints , arXiv:1905.12450 (2019), arXiv:1905.12450 [astro-ph.CO].
- [40] C. Su, H. Shan, J. Zhang, C. Zhao, J. Yu, Q. Wang, L. Xiao, X. Liu, and A. Zhao, *ApJ* **951**, 64 (2023), arXiv:2211.10187 [astro-ph.CO].
- [41] M. Kamionkowski, L. Verde, and R. Jimenez, *J. Cosmology Astropart. Phys.* **2009**, 010 (2009), arXiv:0809.0506 [astro-ph].
- [42] C. D. Kreisch, A. Pisani, C. Carbone, J. Liu, A. J. Hawken, E. Massara, D. N. Spergel, and B. D. Wandelt, *MNRAS* **488**, 4413 (2019), arXiv:1808.07464 [astro-ph.CO].
- [43] N. Schuster, N. Hamaus, A. Pisani, C. Carbone, C. D. Kreisch, G. Pollina, and J. Weller, *J. Cosmology Astropart. Phys.* **2019**, 055 (2019), arXiv:1905.00436 [astro-ph.CO].
- [44] E. Massara and R. K. Sheth, arXiv e-prints , arXiv:1811.03132 (2018), arXiv:1811.03132 [astro-ph.CO].
- [45] S. Nadathur, S. Hotchkiss, J. M. Diego, I. T. Iliev, S. Gottlöber, W. A. Watson, and G. Yepes, in *The Zeldovich Universe: Genesis and Growth of the Cosmic Web*, IAU Symposium, Vol. 308, edited by R. van de Weygaert, S. Shandarin, E. Saar, and J. Einasto (2016) pp. 542–545, arXiv:1412.8372 [astro-ph.CO].
- [46] A. D. Montero-Dorta, A. Balaguera-Antolínez, I. G. Alfaro, A. N. Ruiz, R. K. Sheth, F. Rodríguez, D. Galárraga-Espinosa, C. A. Soto-Suárez, I. Quiroz, and I. Fernández-Sánchez, *A&A* **703**, A58 (2025), arXiv:2504.14616 [astro-ph.CO].
- [47] P. Schneider, J. Ehlers, and E. E. Falco, *Gravitational Lenses* (1992).
- [48] C. Heymans, T. Tröster, M. Asgari, C. Blake, H. Hildebrandt, B. Joachimi, K. Kuijken, C.-A. Lin, A. G. Sánchez, J. L. van den Busch, *et al.*, *A&A* **646**, A140 (2021), arXiv:2007.15632 [astro-ph.CO].
- [49] DES Collaboration *et al.*, *Phys. Rev. D* **105**, 023520 (2022), arXiv:2105.13549 [astro-ph.CO].
- [50] A. Porredon, C. Blake, J. U. Lange, N. Emas, J. Aguilar, S. Ahlen, A. Bera, D. Bianchi, D. Brooks, F. J. Castander, *et al.*, arXiv e-prints , arXiv:2512.15960 (2025), arXiv:2512.15960 [astro-ph.CO].
- [51] C. Sánchez, J. Clampitt, A. Kovacs, B. Jain, J. García-Bellido, S. Nadathur, D. Gruen, N. Hamaus, D. Huterer, P. Vielzeuf, *et al.*, *MNRAS* **465**, 746 (2017), arXiv:1605.03982 [astro-ph.CO].
- [52] Y. Fang, N. Hamaus, B. Jain, S. Pandey, G. Pollina, C. Sánchez, A. Kovács, C. Chang, J. Carretero, F. J. Castander, *et al.*, *MNRAS* **490**, 3573 (2019), arXiv:1909.01386 [astro-ph.CO].
- [53] H. L. Martin, M. J. Hudson, A. Woodfinden, L. Baumont, T. de Boer, P. A. Burger, J. Elvin-Poole, S. Fabbro, S. Farrens, S. Guerrini, *et al.*, arXiv e-prints , arXiv:2507.13450 (2025), arXiv:2507.13450 [astro-ph.CO].
- [54] A. Barreira, M. Cautun, B. Li, C. M. Baugh, and S. Pascoli, *J. Cosmology Astropart. Phys.* **2015**, 028 (2015), arXiv:1505.05809 [astro-ph.CO].
- [55] T. Baker, J. Clampitt, B. Jain, and M. Trodden, *Phys. Rev. D* **98**, 023511 (2018), arXiv:1803.07533 [astro-ph.CO].
- [56] L. Maggione, S. Contarini, C. Giocoli, and L. Moscardini, *A&A* **701**, A55 (2025), arXiv:2504.02041 [astro-ph.CO].
- [57] E. Platen, R. van de Weygaert, and B. J. T. Jones, *MNRAS* **380**, 551 (2007), arXiv:0706.2788 [astro-ph].
- [58] M. C. Neyrinck, *MNRAS* **386**, 2101 (2008), arXiv:0712.3049 [astro-ph].
- [59] R. Boschetti, P. Vielzeuf, M.-C. Cousinou, S. Escoffier, and E. Jullo, *J. Cosmology Astropart. Phys.* **2024**, 067 (2024), arXiv:2311.14586 [astro-ph.CO].
- [60] N. D. Padilla, L. Ceccarelli, and D. G. Lambas, *MNRAS* **363**, 977 (2005), arXiv:astro-ph/0508297 [astro-ph].
- [61] C. T. Davies, M. Cautun, and B. Li, *MNRAS* **480**, L101 (2018), arXiv:1803.08717 [astro-ph.CO].
- [62] M. Cautun, E. Paillas, Y.-C. Cai, S. Bose, J. Armijo, B. Li, and N. Padilla, *MNRAS* **476**, 3195 (2018), arXiv:1710.01730 [astro-ph.CO].
- [63] E. Paillas, M. Cautun, B. Li, Y.-C. Cai, N. Padilla, J. Armijo, and S. Bose, *MNRAS* **484**, 1149 (2019), arXiv:1810.02864 [astro-ph.CO].
- [64] C. Zhao, C. Tao, Y. Liang, F.-S. Kitaura, and C.-H. Chuang, *MNRAS* **459**, 2670 (2016), arXiv:1511.04299 [astro-ph.CO].
- [65] F.-S. Kitaura, C.-H. Chuang, Y. Liang, C. Zhao, C. Tao, S. Rodríguez-Torres, D. J. Eisenstein, H. Gil-Marín, J.-P. Kneib, C. McBride, *et al.*, *Phys. Rev. Lett.* **116**, 171301 (2016), arXiv:1511.04405 [astro-ph.CO].
- [66] M. Bartelmann and M. Maturi, *Scholarpedia* **12**, 32440 (2017), arXiv:1612.06535 [astro-ph.CO].
- [67] M. Shirasaki and M. Takada, *MNRAS* **478**, 4277 (2018), arXiv:1802.09696 [astro-ph.CO].
- [68] E. S. Sheldon, D. E. Johnston, J. A. Frieman, R. Scranton, T. A. McKay, A. J. Connolly, T. Budavári, I. Zehavi, N. A. Bahcall, J. Brinkmann, *et al.*, *AJ* **127**, 2544 (2004), arXiv:astro-ph/0312036 [astro-ph].
- [69] R. Mandelbaum, C. M. Hirata, U. Seljak, J. Guzik, N. Padmanabhan, C. Blake, M. R. Blanton, R. Lupton, and J. Brinkmann, *MNRAS* **361**, 1287 (2005), arXiv:astro-ph/0501201 [astro-ph].
- [70] J. Han, M. Li, W. Jiang, Z. Chen, H. Wang, C. Wei, F. He, J. He, J. Zhang, Y. Liu, *et al.*, *Science China*

- Physics, Mechanics, and Astronomy **68**, 109511 (2025), arXiv:2503.21368 [astro-ph.CO].
- [71] H.-R. Yu, U.-L. Pen, and X. Wang, *ApJS* **237**, 24 (2018), arXiv:1712.06121 [astro-ph.CO].
- [72] D. Inman and H.-R. Yu, *ApJS* **250**, 21 (2020), arXiv:2002.04601 [astro-ph.CO].
- [73] A. Lewis, A. Challinor, and A. Lasenby, *ApJ* **538**, 473 (2000), arXiv:astro-ph/9911177 [astro-ph].
- [74] P. S. Behroozi, R. H. Wechsler, and H.-Y. Wu, *ApJ* **762**, 109 (2013), arXiv:1110.4372 [astro-ph.CO].
- [75] Z. Zheng, A. L. Coil, and I. Zehavi, *ApJ* **667**, 760 (2007), arXiv:astro-ph/0703457 [astro-ph].
- [76] S. Alam, F. D. Albareti, C. Allende Prieto, F. Anders, S. F. Anderson, T. Anderton, B. H. Andrews, E. Armengaud, É. Aubourg, S. Bailey, *et al.*, *ApJS* **219**, 12 (2015), arXiv:1501.00963 [astro-ph.IM].
- [77] S. D. Landy and A. S. Szalay, *ApJ* **412**, 64 (1993).
- [78] F.-S. Kitaura, S. Rodríguez-Torres, C.-H. Chuang, C. Zhao, F. Prada, H. Gil-Marín, H. Guo, G. Yepes, A. Klypin, C. G. Scóccola, *et al.*, *MNRAS* **456**, 4156 (2016), arXiv:1509.06400 [astro-ph.CO].
- [79] A. P. Hearin, D. Campbell, E. Tollerud, P. Behroozi, B. Diemer, N. J. Goldbaum, E. Jennings, A. Leauthaud, Y.-Y. Mao, S. More, *et al.*, *AJ* **154**, 190 (2017), arXiv:1606.04106 [astro-ph.IM].
- [80] M. Jarvis, G. Bernstein, and B. Jain, *MNRAS* **352**, 338 (2004), arXiv:astro-ph/0307393 [astro-ph].
- [81] N. E. Chisari, D. Alonso, E. Krause, C. D. Leonard, P. Bull, J. Neveu, A. S. Villarreal, S. Singh, T. McClintock, J. Ellison, *et al.*, *ApJS* **242**, 2 (2019), arXiv:1812.05995 [astro-ph.CO].
- [82] R. K. Sheth and R. van de Weygaert, *MNRAS* **350**, 517 (2004), arXiv:astro-ph/0311260 [astro-ph].
- [83] S. Hilbert, J. Hartlap, S. D. M. White, and P. Schneider, *A&A* **499**, 31 (2009), arXiv:0809.5035 [astro-ph].
- [84] Z. Chen and Y. Yu, *MNRAS* **534**, 1205 (2024), arXiv:2312.05117 [astro-ph.CO].
- [85] J. Carlson and M. White, *ApJS* **190**, 311 (2010), arXiv:1003.3178 [astro-ph.CO].
- [86] B. Giblin, C. Heymans, M. Asgari, H. Hildebrandt, H. Hoekstra, B. Joachimi, A. Kannawadi, K. Kuijken, C.-A. Lin, L. Miller, *et al.*, *A&A* **645**, A105 (2021), arXiv:2007.01845 [astro-ph.CO].
- [87] M. Gatti, E. Sheldon, A. Amon, M. Becker, M. Troxel, A. Choi, C. Doux, N. MacCrann, A. Navarro-Alsina, I. Harrison, *et al.*, *MNRAS* **504**, 4312 (2021), arXiv:2011.03408 [astro-ph.CO].
- [88] R. Laureijs, J. Amiaux, S. Arduini, J. L. Auguères, J. Brinchmann, R. Cole, M. Cropper, C. Dabin, L. Duvet, A. Ealet, *et al.*, arXiv e-prints , arXiv:1110.3193 (2011), arXiv:1110.3193 [astro-ph.CO].
- [89] D. Z. Liu, X. M. Meng, X. Z. Er, Z. H. Fan, M. Kilbinger, G. L. Li, R. Li, T. Schrabback, D. Scognamiglio, H. Y. Shan, *et al.*, *A&A* **669**, A128 (2023), arXiv:2210.16341 [astro-ph.CO].
- [90] S. Escoffier, M. C. Cousinou, A. Tilquin, A. Pisani, A. Aguichine, S. de la Torre, A. Ealet, W. Gillard, and E. Jullo, arXiv e-prints , arXiv:1606.00233 (2016), arXiv:1606.00233 [astro-ph.CO].
- [91] M. Bonici, C. Carbone, S. Davini, P. Vielzeuf, L. Paganin, V. Cardone, N. Hamaus, A. Pisani, A. J. Hawken, A. Kovacs, *et al.*, *A&A* **670**, A47 (2023), arXiv:2206.14211 [astro-ph.CO].
- [92] J. Buchner, *The Journal of Open Source Software* **6**, 3001 (2021), arXiv:2101.09604 [stat.CO].
- [93] C. Su, H. Shan, C. Zhao, W. Xu, and J. Zhang, *A&A* **699**, A174 (2025), arXiv:2504.15149 [astro-ph.CO].
- [94] G. Aricò, R. E. Angulo, and M. Zennaro, arXiv e-prints , arXiv:2104.14568 (2021), arXiv:2104.14568 [astro-ph.CO].
- [95] A. Spurio Mancini, D. Piras, J. Alsing, B. Joachimi, and M. P. Hobson, *MNRAS* **511**, 1771 (2022), arXiv:2106.03846 [astro-ph.CO].
- [96] J. U. Lange, C. Blake, C. Saulder, N. Jeffrey, J. DeRose, G. Beltz-Mohrmann, N. Emas, C. Garcia-Quintero, B. Hadzhiyska, S. Heydenreich, *et al.*, *The Open Journal of Astrophysics* **7**, 57 (2024), arXiv:2404.09397 [astro-ph.CO].
- [97] C. M. Correa, D. J. Paz, A. G. Sánchez, A. N. Ruiz, N. D. Padilla, and R. E. Angulo, *MNRAS* **500**, 911 (2021), arXiv:2007.12064 [astro-ph.CO].
- [98] C. M. Correa, D. J. Paz, N. D. Padilla, A. G. Sánchez, A. N. Ruiz, and R. E. Angulo, *MNRAS* **509**, 1871 (2022), arXiv:2107.01314 [astro-ph.CO].
- [99] Euclid Collaboration *et al.*, *A&A* **697**, A1 (2025), arXiv:2405.13491 [astro-ph.CO].
- [100] C. Zhao, S. Huang, M. He, P. Montero-Camacho, Y. Liu, P. Renard, Y. Tang, A. Verdier, W. Xu, X. Yang, *et al.*, arXiv e-prints , arXiv:2411.07970 (2024), arXiv:2411.07970 [astro-ph.CO].
- [101] CSST Collaboration *et al.*, arXiv e-prints , arXiv:2507.04618 (2025), arXiv:2507.04618 [astro-ph.IM].
- [102] Ž. Ivezić, S. M. Kahn, J. A. Tyson, B. Abel, E. Acosta, R. Allsman, D. Alonso, Y. AlSayyad, S. F. Anderson, J. Andrew, *et al.*, *ApJ* **873**, 111 (2019), arXiv:0805.2366 [astro-ph].
- [103] Astropy Collaboration, A. M. Price-Whelan, P. L. Lim, N. Earl, N. Starkman, L. Bradley, D. L. Shupe, A. A. Patil, L. Corrales, C. E. Brasseur, *et al.*, *ApJ* **935**, 167 (2022), arXiv:2206.14220 [astro-ph.IM].
- [104] C. R. Harris, K. J. Millman, S. J. van der Walt, R. Gommers, P. Virtanen, D. Cournapeau, E. Wieser, J. Taylor, S. Berg, N. J. Smith, *et al.*, *Nature* **585**, 357 (2020).
- [105] J. D. Hunter, *CiSE* **9**, 90 (2007).
- [106] P. Virtanen, R. Gommers, T. E. Oliphant, M. Haberland, T. Reddy, D. Cournapeau, E. Burovski, P. Peterson, W. Weckesser, J. Bright, *et al.*, *Nature Methods* **17**, 261 (2020).
- [107] A. Lewis, *J. Cosmology Astropart. Phys.* **2025**, 025 (2025), arXiv:1910.13970 [astro-ph.IM].
- [108] J. M. Zorrilla Matilla, S. Waterval, and Z. Haiman, *AJ* **159**, 284 (2020), arXiv:1909.12345 [astro-ph.CO].
- [109] F. Vecchi, D. Harvey, J. Nightingale, M. Schaller, J. Schaye, and E. Tregidga, *A&A* **703**, A45 (2025), arXiv:2509.13403 [astro-ph.CO].